Article

Finite Element Analysis of Microwave Tumor Ablation Based on Open-Source Software Components

Nikola Bošković [ID], Marija Radmilović-Radjenović *[ID] and Branislav Radjenović

Institute of Physics, University of Belgrade, Pregrevica 118, 11080 Belgrade, Serbia; nikolab@ipb.ac.rs (N.B.)
* Correspondence: marija@ipb.ac.rs

Abstract: Microwave ablation is a procedure for treating various types of cancers during which a small needle-like probe is inserted inside the tumor, which delivers microwave energy, causes tissue heating, and effectively produces necrosis of the tumor tissue. Mathematical models of microwave ablation involve the modeling of multiple physical phenomena that occur during the procedure, including electromagnetic wave propagation, heat transfer, and tissue damage. In this study, a complete model of a microwave ablation procedure based on open-source software components is presented. First, the comprehensive procedure of mesh creation for the complete geometric arrangement of the microwave ablation, including a multi-slot coaxial antenna, a real liver tumor taken from the database, and the surrounding liver tissue, is described. It is demonstrated that utilizing smart meshing procedures significantly reduces the usage of computational resources and simulation time. An accurate custom explicit Euler time loop was designed to obtain temperature values and estimate tissue necrosis across the computational domain during the time of microwave ablation. The simulation results obtained by solving the electromagnetic field using the finite element method in the frequency domain are presented and analyzed. The simulation was performed for a microwave frequency of 2.45 GHz, and the volumetric distribution of temperature and estimation of cell damage over 600 s are presented.

Keywords: computational physics; microwave ablation; necrotic tissue; open-source software

MSC: 92-10

1. Introduction

Microwave ablation (MWA) has been shown to be effective in treating certain types of cancer, including liver, lung, and kidney tumors [1–4]. It is a minimally invasive medical procedure with a short recovery time, making it a viable alternative to traditional surgical methods [5–7]. During MWA, a small needle-like probe is inserted into the tumor, and microwave energy is delivered to heat and destroy cancer cells [8,9]. Multi-slot coaxial antennas are commonly used for the delivery of microwave radiation because of their simplicity, low complexity, and ability to generate highly spherical ablation zones [10,11]. To improve the safety and efficacy of the procedure, modeling MWA is an important tool for predicting the size and shape of the ablation zone and optimizing treatment for individual patients [12,13].

Modeling MWA as a multiphysics problem involves modeling multiple physical phenomena that occur during the procedure, including electromagnetic wave propagation, heat transfer, and tissue damage [14,15]. These phenomena are interrelated, and modeling them together can provide a more accurate and comprehensive understanding of tissue behavior during the procedure [16,17]. The first stage encompasses the accurate modeling of the microwave radiation of the antenna. The second stage involves modeling the interaction between tissue and antenna radiation and heat transfer under the influence of blood flow effects. The third stage requires an estimation of cell death due to heating. While

the material parameters of the antenna components can generally be observed as constant during ablation, the material properties of the healthy tissue and tumor are temperature (time) dependent [18,19]. Tumor shape is patient-specific, so a general approach using a spherical or static tumor model is inaccurate [20]. The water concentration in the tissue changes with increasing temperature, effectively altering the physical properties of the tissue [21,22].

From a numerical modeling perspective, modeling MWA represents a closed boundary problem with the required results in a narrow frequency bandwidth [23]. The three-dimensional (3D) finite element method (FEM) is an excellent choice for solving all the required electromagnetic and heat transfer equations, as implemented in widely used software such as the COMSOL Multiphysics simulation package [24,25]. Ideal software solutions for MWA practitioners should enable users to input tumor scan data obtained from the computerized tomography (CT) scan of a patient [26], select the probe model with the antenna from the available library, and set the input power and geometric location of the probe inside the tumor. Commercially available packages can be used to develop such a solution, but software based on open-source code would be far more beneficial [27–30], since commercially based packages typically have high price and usage limitations.

Physical processes can be described using partial differential equations (PDE). FEM is a numerical method in which the PDE is numerically converted into a set of linear algebraic equations to obtain approximate solutions for a specific physical problem [31]. In FEM, the geometry is divided into many small subdomains, known as finite elements, on which the approximation of the unknowns can be performed using simple functions. The division of the geometry into finite elements is called meshing [32]. The two basic types of FEM meshing are unstructured and structured meshing. Mixed meshing, with a combination of these two types of meshing with the same geometry, is also possible. Solving the PDE using the finite element method requires computational resources, which are directly governed by the number of elements and quality of the finite element mesh.

In this paper, we present a complete model of the MWA procedure based on open-source software components, which was one of the most important goals. We shall describe the comprehensive procedure of mesh creation of the complete MWA geometric arrangement, including a multi-slot coaxial antenna, a real liver tumor taken from the database [26], and surrounding liver tissue. We used a smart meshing procedure to significantly reduce the use of computational resources and simulation time. For geometry and mesh creation, we used Gmsh, an open-source package that implements multiple state-of-the-art solutions for automatic mesh creation [33–43]. Gmsh can create complex geometries using the OpenCASCADE computer-aided design (CAD) engine [44]. The mesh created with Gmsh can be used with many FEM solvers, but the most suitable is a general FEM solver called GetDP [45,46]. It is free and developed by the same team that works on Gmsh, and it is a compiled bundle with Gmsh in the Open Numerical Engineering LABoratory (ONELAB), an open-source, lightweight interface for finite element software [47]. We designed an accurate custom explicit Euler time loop to obtain temperature values and estimate tissue necrosis across the computational domain during MWA. Finally, the simulation results obtained by solving the electromagnetic field with FEM in the frequency domain will be presented and analyzed.

2. Methodology

The proposed solution consists of implementing the physics of the MWA procedure, generating geometry, and meshing in a form suitable for FEM simulation. We show these methods in this section.

2.1. Physics of the MWA Procedure

In MWA, the electromagnetic field and tissue heating are coupled. To model MWA, we first need to calculate the electromagnetic field distribution originating from the antenna and spread across the computational domain. Human tissues have approximately equal

magnetic properties, and the MWA process is performed through electric field interaction; hence, we need to calculate only the electric field distribution. The calculated field was then used as an external heat source in the bio-heat equation [48]. Tissue heating is a slow process that can occur within a few seconds. In comparison, electric field propagation is extremely fast and occurs in nanoseconds; therefore, we calculated the electric field in the frequency domain and used the results to calculate the temperature distribution in the time domain. Subsequently, we estimated the fraction of necrotic tissue over time during MWA.

2.1.1. EM Field Calculations

The MWA system electromagnetic field generated by the antenna is usually described by the well-known frequency domain wave equation for electric field, derived from Maxwell's equations [31], given as:

$$\nabla^2 \vec{E} - \mu_r k_0^2 \left(\varepsilon_r - \frac{j\sigma}{\omega \varepsilon_0} \right) \vec{E} = 0, \tag{1}$$

where μ_r is the relative permeability (its value is 1 for a non-magnetic environment), $\omega = 2\pi f$ is the angular frequency, $\vec{E}$ is the electric field vector generated by the antenna, σ is the electric conductivity, ε_0 is the permittivity of vacuum, and k_0 is the vacuum propagation constant.

Propagation of the electric field in coaxial cable in cylindrical coordinate system can be expressed as:

$$\vec{E} = \vec{e_r} \frac{C}{r} e^{j(\omega t - kz)}, \tag{2}$$

where z is the direction of propagation, $\vec{e_r}$ is the radial vector, r is the radius, and C represents a constant that can be expressed as:

$$C = \sqrt{\frac{Z P_{av}}{\pi \ln \frac{r_0}{r_i}}}, \tag{3}$$

$$Z = \frac{1}{2\pi} \sqrt{\frac{\mu}{\varepsilon}} \ln \frac{r_0}{r_i}, \tag{4}$$

where P_{av} is the time-averaged power flow in the cable, Z is the impedance of the coaxial cable, r_0 and r_i are the outer and inner radii of the dielectric, respectively; μ is the permeability and ε is the permittivity.

The boundary condition on the conductor surface is given by $\vec{n} \times \vec{E} = 0$. This represents the PEC boundary condition; the tangential component of the electric field is zero, only the normal component exists, and it is perfectly reflected from the boundary. The electric field does not penetrate the volume within the PEC boundary; hence, such a volume is of no interest in electric-field calculations.

The SAR represents the amount of radiation absorbed by a tissue [25]. It can identify which part of the tissue will be the most affected by radiation and how the electric field propagation interacts with the tissue. It can be determined from the electric field, electric conductivity σ, and density of the observed domain ρ, as follows:

$$SAR = \frac{\sigma}{2\rho} \left| \vec{E} \right|. \tag{5}$$

The scattering parameter S_{11} is one of the fundamental parameters of antennas. This parameter represents the extent to which the antenna matches the power source. A value below -10 dB at the working frequency was considered good. A high S_{11} value is dangerous in MWA for both the equipment and patients. The power source can be damaged, and antenna conductors can produce very high temperatures, essentially burning tissue in close

proximity, whereas radiation can be very poor. It can be calculated by solving the surface integral at the port boundary as follows [25]:

$$S_{11} = \frac{\iint\limits_{PORT} \left(\vec{E} - \vec{E}_{PORT} \right) \cdot \vec{E}_{PORT}^* dS}{\iint\limits_{PORT} \vec{E}_{PORT} \cdot \vec{E}_{PORT}^* dS}, \tag{6}$$

where $\vec{E}$ is the electric field vector calculated in the observed domain, $\vec{E}_{PORT}$ is the electric field vector defined at the port, and its conjugate is $\vec{E}_{PORT}^*$ [25].

The wave Equation (1) is in its strong form and generally has no closed-form solution. Such a formulation cannot be used in FEM approach [31], and it needs to be written in so-called weak form, where the weak solution satisfies the integral equation when "tested" with a well-defined set of test functions:

$$\iiint\limits_{V} \left[(\nabla \times W) \cdot \frac{1}{\mu_r} \cdot \left(\nabla \times \vec{E} \right) - W \cdot k_0^2 \left(\varepsilon_r - \frac{j\sigma}{\omega \varepsilon_0} \right) \vec{E} \right] dV - \iint\limits_{S} W \cdot \left[\vec{n} \times \left(\frac{1}{\mu_r} \nabla \times \vec{E} \right) \right] dS = 0, \tag{7}$$

where W represents the weighting test function, V is the volume in which the electric field calculation is performed, S is the surface boundary of V, and $\vec{n}$ is the unit normal vector. Here, S represents the combination of the port boundary surface and absorbing boundary surface (ABS). Here, $\mu_r = 1$ and the second part of (7) can be written as an absorbing boundary condition [31]:

$$\iint\limits_{ABS} W \cdot \left[\vec{n} \times \left(\nabla \times \vec{E} \right) \right] dS + \iint\limits_{ABS} W \cdot \left[jk_0 \sqrt{\varepsilon_r} \cdot \left[\vec{n} \times \left(\vec{n} \times \vec{E} \right) \right] \right] dS = 0. \tag{8}$$

Similarly, the port boundary condition defined at the port surface can be written as [31]:

$$\iint\limits_{PORT} W \cdot \left[\vec{n} \times \left(\nabla \times \vec{E} \right) \right] dS + \iint\limits_{PORT} W \cdot \left[jk_0 \sqrt{\varepsilon_r} \cdot \left[\vec{n} \times \left(\vec{n} \times \vec{E} \right) \right] \right] dS + \iint\limits_{PORT} W \cdot \left[2jk_0 \sqrt{\varepsilon_r} \vec{E}_{PORT} \right] dS = 0. \tag{9}$$

By solving the previous equations, we can obtain a FEM approximation of the electric field vector in the defined volume.

2.1.2. Heat Transfer Calculation

The transfer of the heat generated by the electromagnetic field in MWA is described by Pennes's bio-heat equation [48]:

$$\rho c \frac{\partial T}{\partial t} = \nabla \cdot (k \nabla T) + \rho_b \omega_b c_b (T_b - T) + Q_{ext} + Q_{met}, \tag{10}$$

where t is the time, ρ, c, and T are the density, specific heat capacity, and temperature of the tissue, respectively. ρ_b, c_b, and ω_b are the density, specific heat capacity, and perfusion rate of the blood, $T_b = 37\,^\circ\text{C}$ denotes the arterial blood temperature, Q_{met} is the metabolic heat, and Q_{ext} represents the external heat source. Q_{ext} represents the heat generated from MWA, and considering that $Q_{ext} \gg Q_{met}$, in practical MWA use cases, Q_{met} can be neglected. The coupling with an electric field is given as:

$$Q_{ext} = \frac{\sigma \left| \vec{E} \right|^2}{2}, \tag{11}$$

where σ is electrical conductivity of the tissue. The dependence of the thermal conductivity of the tissue k on the temperature is given by the following relation [10,14]:

$$k(T) = k_0 + \Delta k |T - T_0|, \tag{12}$$

where k_0 is the thermal conductivity of the tissue measured at temperature T_0 and $\Delta k = 0.001161$ (K^{-1}) characterizes the change in k as a function of temperature. The blood perfusion rate is assumed to stop when coagulation occurs above 60 °C and is expressed as [10]:

$$\omega_b(T) = \begin{cases} 0.000021 \cdot T + 0.0035, & T \leq 60\,°\text{C} \\ 0, & T > 60\,°\text{C} \end{cases}. \tag{13}$$

A heterogeneous model of blood perfusion [49,50] based on clinical measurements [51,52] can give a more accurate MWA calculation. Liver tissue contains a high concentration of water (approximately 78%). Owing to the rise in temperature during MWA, a change in water content occurs and can be expressed as [53]:

$$W(T) = \begin{cases} 0.778 \cdot \left(1 - e^{\frac{T-106}{3.42}}\right), & 70\,°\text{C} \leq T \leq 100\,°\text{C} \\ 7.053 - 0.064096 \cdot T, & 100\,°\text{C} \leq T \leq 104\,°\text{C} \\ 0.778 \cdot e^{-\frac{T-80}{34.37}}, & T > 104\,°\text{C} \end{cases}. \tag{14}$$

Above 100 °C, the evaporation of water content may decrease concentration of the water to less than 20%, which will cause a significant change in all tissue parameters. Hence, the specific heat capacity used in (10) should be replaced with an effective value [54]:

$$c' = c - \frac{\alpha}{\rho} \frac{\partial W}{\partial T}, \tag{15}$$

where $\alpha = 2{,}260{,}000$ (J/kg) is the water latent heat constant, ρ is the water density, and c is the specific heat of the tissue.

Based on Equations (15) and (12), the specific heat capacity and thermal conductivity in relation to the temperature change are calculated and shown in Figure 1a. Values of the specific heat capacity and thermal conductivity in tumors are around 10% higher than the ones in the liver tissue. This is beneficial for the processes of MWA because, under the same conditions, tumor tissue will heat faster than liver tissue. Thermal conductivity is a simple linear function of the temperature. Based on Equation (13), the blood perfusion rate in relation to the temperature is given in Figure 1b.
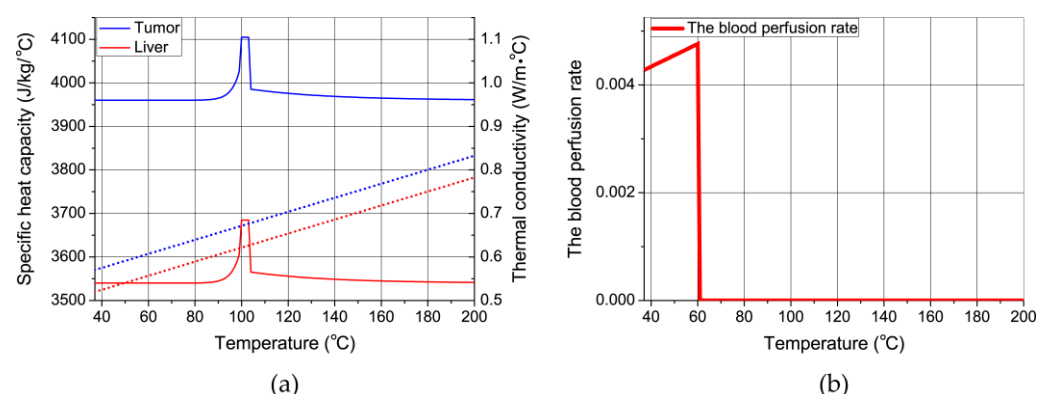

Figure 1. (**a**) Change in the specific heat capacity (full line) and thermal conductivity (dots) with the temperature. (**b**) Change in the blood perfusion rate with the temperature.

Specific heat capacity below 70 °C is constant; above 70 °C due to change in water content, there is a rise with a maximum value between 100 °C and 104 °C, and above 104 °C, specific heat capacity becomes stable again.

The dielectric constant of the tissue ε_r and electrical conductivity σ can be expressed as [14]:

$$\varepsilon_r = a_1 \cdot \left(1 - \frac{1}{1 + e^{(a_2 - a_3 T)}} \right), \tag{16}$$

$$\sigma = b_1 \cdot \left(1 - \frac{1}{1 + e^{(b_2 - b_3 T)}} \right). \tag{17}$$

The values of the coefficients in Equations (16) and (17) are given in Table 1.

Table 1. Values of the coefficients used in the calculation of ε_r and σ for the liver tissue and tumor.

Coefficients	Tissue	
	Liver	Tumor
a_1	44.3	54.8
a_2	5.223	5.223
a_3	0.0524	0.0524
b_1	1.69	2
b_2	6.583	6.583
b_3	0.0598	0.0598

Tissue damage is a function of temperature and time, and can be approximated using the Arrhenius equation [55,56]:

$$\frac{\partial \Omega}{\partial t} = A e^{\left(-\frac{\Delta E}{RT} \right)}, \tag{18}$$

where $A = 7.39 \times 10^{39}$ 1/s and $\Delta E = 2.577 \times 10^5$ J/mol represent the frequency factor and activation energy for the irreversible damage reaction, respectively; T is the temperature calculated at each point of the model region, and R is the universal gas constant. By solving differential Equation (18), the fraction of necrotic tissue can be calculated as follows [55,56]:

$$\theta_d = 1 - e^{-\Omega}. \tag{19}$$

From Equation (19), a value of 1 represents total tissue damage, and a value of 0 indicates that there is no damage. The values of the thermo-physiological parameters used in this work are given in Table 2.

Table 2. Thermo-physiological parameters used in this work.

Parameter	Tissue		
	Liver	Tumor	Blood
Density, [kg/m^3]	1079	1040	1060
Specific heat, [J/kg/°C]	3540	3960	3600
Thermal conductivity, [W/m·°C]	0.52	0.57	0.5

2.2. Geometry and Mesh Generation

Gmsh comprises two modules for geometry creation. The built-in module requires model creation from lower to higher dimensions (points < curves < surfaces < volumes). However, for complex structures, this type of modeling can quickly get out of control. The OpenCASCADE module supports work with solids and has the same capabilities as any commercially available CAD design package. Three-dimensional models can be directly composed of defined volumes, and the most important factor is complete Boolean support, which means that multiple solid models can be united and intersected, effectively creating new volumes. Geometry can be manipulated in any way: translated, rotated, copied, scaled, and so on. The OpenCASCADE module supports the import, export, and processing of the STEP and IGES file formats, which are commonly used 3D geometry formats, and the BREP file format, which is native to OpenCASCADE.

The Gmsh mesh module is extremely versatile and powerful. Gmsh can operate with most standard FEM shapes, such as lines, triangles, quadrangles, tetrahedrons, hexahedrons, prisms, and pyramids [32,33], as shown in Figure 2. The standard Gmsh unstructured mesh algorithm comprises planar (2D) elements that are generally meshed with triangles (some structures can be recombined into quadrangles), whereas 3D elements are meshed with tetrahedrons or tetrahedrons and pyramids when quadrangles are present [43].
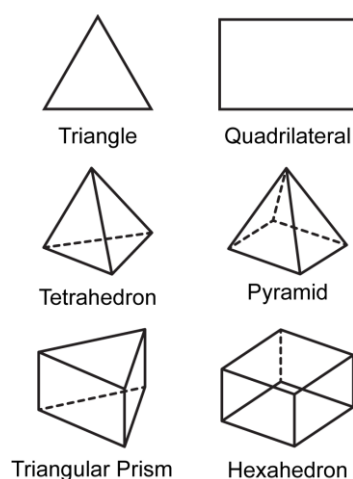

Figure 2. Standard FEM shapes: two-dimensional (triangle and quadrilateral) and three-dimensional (tetrahedron, pyramid, triangular prism, and hexahedron).

Global control of the mesh size can be achieved by specifying the minimal and maximal cell sizes that can be specified at any point, curve, volume, etc. The mesh can be interpolated linearly at the geometric edge or with geometric progression. The mesh size can be adapted to the geometric curvature. The quality of each created element is determined, and appropriate adaptive and refinement algorithms can be applied. An equilateral triangle has a quality of 1, and a degenerated shape with a zero area has a quality of 0. Similarly, for a tetrahedron, the maximum quality is obtained when the tetrahedron is constructed from equilateral triangles, whereas zero quality occurs when the element is shattered and has zero volume.

The major advantage of unstructured meshing is that it can be applied to any shape. However, for good quality meshing, multiple refinement steps are often necessary, with a massive increase in the number of elements, computing time, and resource demands, and generally lower accuracy in FEM simulations in comparison with structured meshing. Hexahedrons with small aspect ratios are ideal mesh elements in FEM and should be used whenever possible. Some geometrically highly irregular structures, such as tumors, are difficult to represent using this algorithm, whereas probes with antennas can be represented using structured meshing. There are numerous advantages of structured meshing in FEM simulations. The number of elements in the same structure with structured meshing was several times smaller. With accurately defined structured meshing, mesh quality is superior, mesh generation is very quick because the best quality mesh is already defined, and there is no need for multiple refinement steps.

In MWA, the liver represents the computational domain where the process of MWA takes place, as seen in Figure 3a. In MWA, we are interested in simulating the processes around the tumor, which is usually much smaller than the entire liver volume; hence, the computational domain does not have to consider the whole liver, and it can be a part of the liver around the tumor in the form of a regular geometrical shape. The most commonly used shape is a cylinder. However, for structured meshing, the hexahedron domain is a better choice because of the possibility of using mostly identical hexahedrons as finite elements across the entire domain. Two models were developed in this study. One had

an unstructured tetrahedral mesh and a cylindrical computational domain with a radius of 30 mm and height of 90 mm, and the other had a mixed meshing and hexahedral computational domain with dimensions of 60 mm × 60 mm × 90 mm.
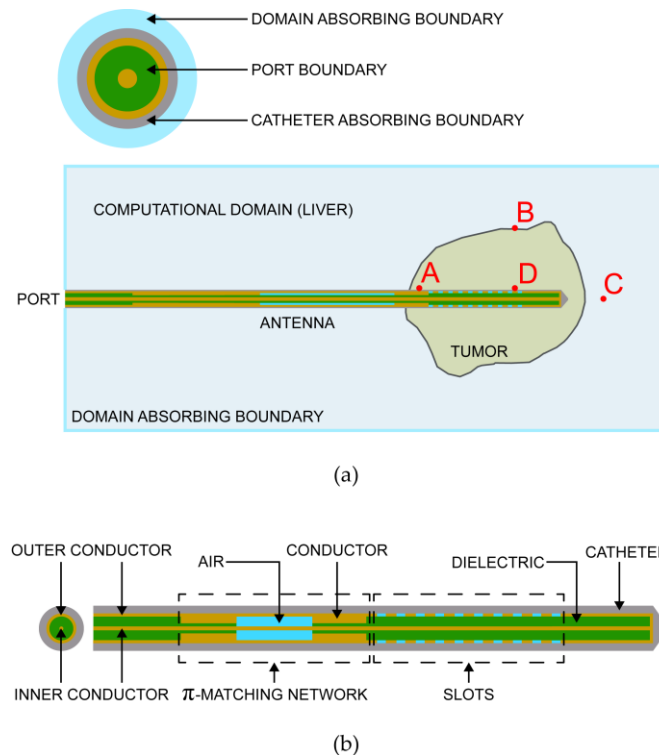

(a)

(b)

Figure 3. (**a**) Geometry of the problem, points A, B, C, and D are used as a reference in the simulation algorithm, and (**b**) probe with the antenna geometry.

Figure 3b shows the geometry of the probe used for MWA [10,13]. The antenna was a coaxial slot antenna, where the inner conductor passed through the center of the geometry and was connected to the outer conductor at the end of the antenna. Radiation occurred through 10 slots in the outer conductor. A matching network exists in front of the radiating slots. The entire antenna is placed inside the catheter. There are four different material regions in the probe structure: the metal conductor, the dielectric in the antenna between conductors, air, and the dielectric material of the catheter (Table 3). The basic geometry of the antenna was a long cylindrical volume. From electromagnetic analysis through the FEM, the value of the electric field is necessary for heat transfer estimation. From electromagnetic theory, we can assume that there is no field propagation inside the conductor volume, and that the faces of the conductor volume behave as field boundaries. Field propagation occurs only through dielectric materials. Based on this, there is no need for volume meshing of the conductor part; therefore, the basic geometry for the meshing of the antenna consists of multiple concentric hollow cylinders.

Table 3. Materials used in the probe construction.

Material	Dielectric Constant
Air	1
Dielectric	2.05
Catheter	2.1

An arbitrary hollow cylinder is shown in Figure 4. Using the OpenCASCADE module, the geometry can be created with a few commands, and the cylinder can be defined by specifying its position in space, radius, and height. All other geometric components of lower

orders, such as surfaces, curves, and nodes, were automatically created. All elements of the same order have unique tags in Gmsh that are necessary for any geometrical manipulation.
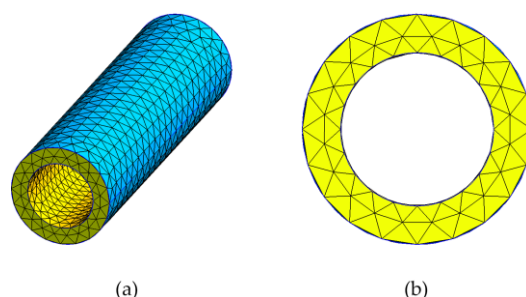

(a)   (b)

Figure 4. Unstructured meshing of a cylinder with dimensions of 1 mm, 1.5 mm, and 10 mm for the inner radius, outer radius, and length, respectively. (**a**) Volume view and (**b**) planar projection view.

The construction of the unstructured mesh was simple. It can be seen that the mesh from the curvature is 20, which means that the circular cross-section is represented by 20 segments, which is sufficient for an accurate circle geometry representation, and the maximal size of the cells is specified at 2 mm. The number of tetrahedrons in the volume per quality factor is listed in Table 4. After the two mesh optimization steps, the mesh became suitable for the simulation. In the second iteration, all elements with a quality lower than 0.3 are eliminated, and the average mesh quality is now 0.76, which is very good. The mesh contained 3969 tetrahedrons and 2704 triangles.

Table 4. The number of elements in a specific quality factor range in two mesh iterations shown in Figure 4.

Quality Factor Range	Number of Elements per Iteration	
	First	**Second**
0.0–0.1	8	0
0.1–0.2	15	0
0.2–0.3	4	0
0.3–0.4	13	13
0.4–0.5	30	28
0.5–0.6	92	87
0.6–0.7	1235	1232
0.7–0.8	1493	1502
0.8–0.9	327	328
0.9–1.0	779	779

Structured meshing cannot be applied directly to arbitrary geometries. The basic condition in Gmsh is that the volume must have five or six faces. Neighboring volumes must follow a defined grid pattern. Geometric volumes must be sliced or adjusted to conform to the structured meshing. In this case, the geometry has four faces. The simplest way to conform this geometry to structured meshing is to slice the geometry through the symmetry plane to form two half-ring volumes, as shown in Figure 5a. Instead of a full cylinder, two symmetrical half-cylinders were created, each with six faces, as displayed in Figure 5b.

The number of segments per curve has to be specified for each plane. The desired meshing parameters were the same as before, with 20 segments for circular representation and a maximal cell size of 2 mm. There are no automatic meshing algorithms for structured meshing; however, the process of specifying the number of segments per curve can be easily automated with simple scripting. There are various options for dividing the physical length of the residual curves by 2 mm; therefore, the number of segments can be obtained. The curves that define the half circumference should be divided into 10 segments. We obtained a meshing composed of 250 quadrangles and 100 identical hexahedrons. The base

of the hexahedron had a very small deviation from the rectangle, and the structure was elongated in a single direction. The mesh quality of this element was close to perfect.
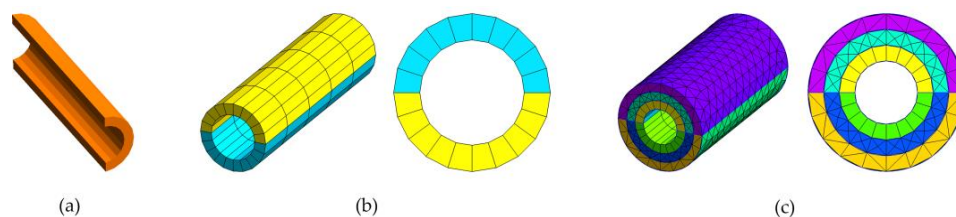

(a)   (b)   (c)

Figure 5. (**a**) Half-ring volume, (**b**) two half-ring volumes with structured meshing, and (**c**) volume with a combination of structured meshing, unstructured meshing, and mixed meshing.

The difference in the number of finite elements for these two types of meshing is large. In unstructured meshing, there are 11 times more planar elements and 40 times more volume elements. All volume elements in the structured elements are identical, which is highly desirable, and the mesh quality is superior, resulting in a shorter simulation time, smaller resource usage, and higher accuracy. In this simple example, it is clear that there is a significant benefit to using structured meshing.

In Gmsh, it is possible to combine both structured and unstructured meshing with a transitional layer of pyramids between hexahedrons and tetrahedrons. In this model, the tumor represents an irregular unpredictable geometry, which is meshed with unstructured meshing, and the catheter volume layer is between the antenna and the tumor and can have a layer of pyramids. Figure 5c shows an example of a hollow cylinder comprising an internal ring meshed with structured meshing (hexahedrons) and an outer ring meshed with unstructured meshing. The middle ring contains pyramids, which are transitional layers between two types of meshing.

The geometry of the probe can be simply constructed as a group of solid objects directly in Gmsh based on the antenna dimensions. The geometry is clearly defined and does not change during the analysis. Tumor geometry can be obtained from medical scans in the STL format, which represents an object in the form of a shell made from multiple triangles [17,32]. STL geometry represents the surface meshing of an object with triangles. The STL file does not represent solid geometry; therefore, it cannot be used with OpenCASCADE. The built-in module can work with the STL format and create a surface and volume geometry based on it, after which meshing can be performed. The geometry of STL files typically has a very high resolution and can consist of a very large number of triangles. A tumor is a live structure with blood circulation and other metabolic processes, and its geometry can undergo slow and fast changes over time. For the purpose of accurate simulation of MWA, extremely high resolution is not required as long as the tumor volume boundaries are accurately represented.

In Gmsh, it is possible to use STL remeshing, where the surface geometry can be reconstructed in a much smaller number of triangles with higher mesh quality. In Figure 6a, an STL file of the live liver tumor with the dimensions of 21.9 mm × 22.7 mm × 25.4 mm is shown. The original model contained 3000 triangles. Remeshing can be performed, depending on the required resolution. In Figure 6b, one version of remeshing is shown, with 1122 triangles. With all the details, this model provides a good representation of the tumor for adequate analysis. In Figure 6c, the more aggressive remeshing model has 336 triangles, and some details are lost. The number of smaller triangles is decreased; hence, the resolution is lower, but the basic geometry is still present.

The built-in Gmsh module can create the geometry and mesh for the STL file, but it does not support Boolean operations. The geometry of the probe with the antenna is inserted into the tumor, and the tumor is inside the liver tissue, so new geometries must be created based on the interaction of the probe, tumor, and liver tissue. Therefore, it was necessary to use the OpenCASCADE module. For this, STL must be converted to a format that is suitable for the OpenCASCADE module, such as the BREP file format. In Gmsh,

there is no direct way for STL conversion, but it can be achieved through external scripting, for example, with the Python API. The BREP file of the tumor can then be imported and used to create a solid volume that can be used in the OpenCASCADE module as any other solid geometry.
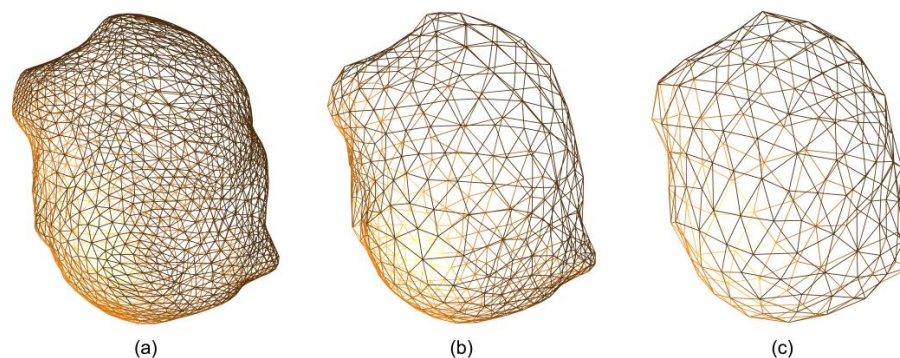

Figure 6. (**a**) STL representation of the tumor: (**a**) original with 3000 triangles, (**b**) remeshed with 1122 triangles, and (**c**) remeshed with 336 triangles.

A very important operation for simulation preparation is grouping finite element volumes and surfaces based on whether they belong to a particular material or have the same boundary conditions. Each material listed in Table 3 belonged to a unique physical zone. In addition, there are tumor and liver volumes; hence, there are five physical volume zones. There is no electric field in the conductor; hence, the volume meshing of the conductors is not required.

There are three specific surface boundary regions: absorbing, port, and Perfect Electric Conductor (PEC) boundaries. The largest is the absorbing boundary, which consists of two parts: the surface at the exterior of the computational domain (liver) (Figure 3a) and a small ring surface at the exterior of the catheter, which represents the catheter's absorbing boundary. The absorbing boundary has a very important purpose in the FEM simulation. The electric field intensity decreases with distance from the source; for infinite or very large domain spaces (relative to wavelength), the entire electric field is negligible, and there is no reflection from domain surface boundaries. The purpose of the absorbing boundary is to absorb the electric field, which essentially enables the small computational domain to behave in a manner similar to that of a much larger domain (the entire liver).

The port boundary was defined as the planar ring surface on the exterior of the antenna dielectric (Figure 3a). This is where the electric-field source is defined. The conductor surfaces played a major role in the simulation. This essentially represents a reflective boundary that controls the direction of propagation of the electric field. The PEC boundary is a region consisting of surface zones at the interface between the dielectric and the conductors. Three surface zones define the PEC interface: the antenna dielectric conductor, air conductor, and catheter conductor.

The frequency of interest here is 2.45 GHz, and the approximate value of the dielectric constant for the liver tissue is 44, which indicates that the finite element size in the given domain should be $\lambda_g/10 \approx 2$ mm. The dielectric constant is a critical parameter for electromagnetic simulations. A higher value of the dielectric constant requires a higher meshing density.

Figure 7a shows a cylindrical domain cross-section with the probe (dark), tumor (yellow), and liver (blue). The total volume of the domain was 254.47 cm^3, and the total number of tetrahedrons was 640,604. In Figure 7b, we show a view of the location where the probe with the antenna exits the domain. The conductors are not meshed. The inside parts of the geometry can be seen: air (green), which is further inside, and the catheter (purple), which is at the end of the antenna. The port boundary surface (orange) and the absorbing boundary of the catheter (red) are shown. The blue surface around the catheter represents the absorbing boundary of the domain on the exterior of the liver.
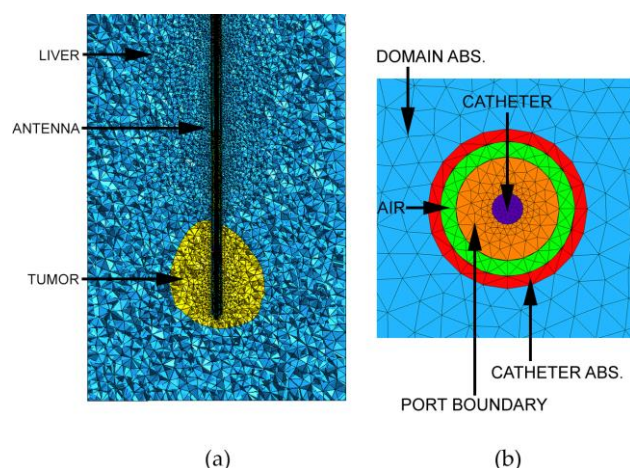
Figure 7. The geometry of the unstructured meshing shown in Figure 3; the cylindrical domain radius was 30 mm, and the height was 90 mm. (**a**) Cross-sectional top view (tumor zone is yellow, liver domain is blue, and antenna is dark) and (**b**) projection view of the port surface.

As shown in Figure 8, the model has a hexahedron domain meshed with a combination of structured and unstructured meshing. The total volume of this domain was 324 cm^3, which was 27% higher than that of the cylindrical domain. The total number of hexahedrons was 49,552 (green), the total number of tetrahedrons was 99,063 (red), and the total number of pyramids was 2709 (blue). Even with larger volumes, the total number of volume elements is much smaller; the number of tetrahedrons is 6.46 times smaller, and the total number of volume elements is 4.38 times smaller. The hexahedrons used in the domain are mostly identical cubes, which are perfect elements for FEM analysis. For higher mesh control in the geometry, we can create dummy objects whose purpose is to facilitate a specific mesh pattern. Around the tumor, a dummy hexahedron volume is created; the volume was meshed with tetrahedrons (red) in the same manner as the tumor, which enabled a smooth transition to structured meshing (Figure 8a). A similar dummy object was placed around the catheter, as shown in Figure 8b,c. The catheter was meshed with a small layer of pyramids intertwined with surrounding tetrahedrons. The boundary regions are the same as those shown in Figure 7b.
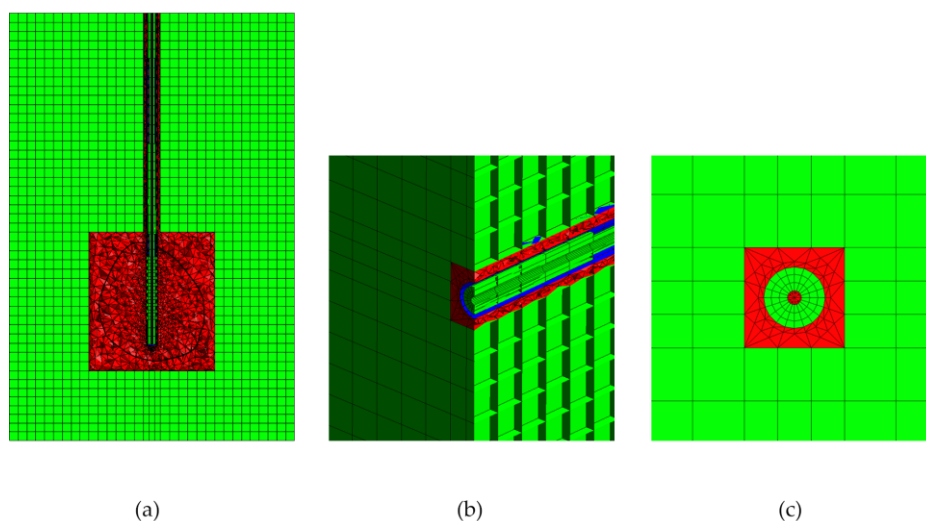

Figure 8. Mixed meshing of the geometry from Figure 2, a hexahedral domain with dimensions of 60 mm × 60 mm × 90 mm. (**a**) Cross-sectional top view: the tumor zone is marked with a black line, and meshing is performed with three types of geometry: hexahedrons (green), tetrahedrons (red), pyramids (blue), (**b**) cross-sectional side view and (**c**) projection view at the port surface.

3. Results

Solving the previously defined equations in the domain of interest with the FEM was performed using GetDP. The mesh generated by Gmsh contains a list of nodes with their coordinates, a list of finite elements with defined element type (line, triangle, quadrangle, tetrahedron, hexahedron, prism, etc.) with a number tag characterizing the physical region to which a particular element belongs and the list of its nodes. The only necessary connection between the mesh and the GetDP is a unique tag of the physical zone defined in the mesh and linked as a group of regions inside the GetDP [45]. All physical definitions were expressed in the GetDP scripting language. All the volume physical zones are joined in a group called a domain. Additionally, the liver and tumor tissues were grouped into a heat zone. We can configure the temperature to only be calculated in the heat zone because we are only interested in the tissue temperature. By solving the electric field vector in the frequency range of 2 GHz to 3 GHz and using Equation (6), we can obtain the values of S_{11} versus the frequency, as can be seen in Figure 9. Simulations were carried out for the models in Figures 7 and 8, with unstructured and mixed meshing, respectively. We can see that S_{11} values in both cases are quite similar, and the antenna has good reflection below -10 dB at 2.45 GHz. The rest of the analyses is focused only on a frequency of 2.45 GHz and an input power of 13 W.
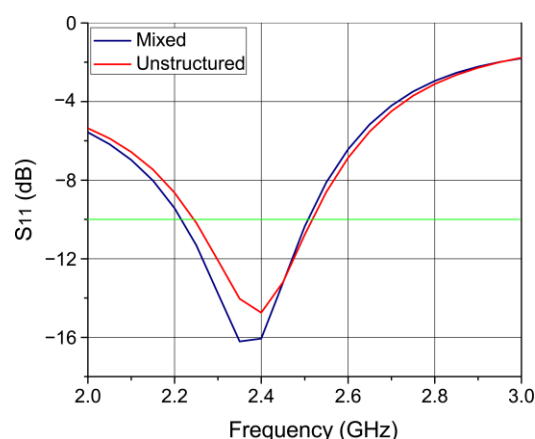

Figure 9. S_{11} parameters at the antenna port for unstructured meshing (Figure 7) and mixed meshing (Figure 8). Green horizontal line represents -10 dB limit.

To obtain the temperature originating from MWA, we must acquire the value of the electric field across the domain and use it as an external source in the bio-heat Equation (10). Solving these coupled equations is challenging. The best approach is to solve the equations for the electric field and then use the solution in the bio-heat equation. In this manner, there is no difference in solving coupled problems compared to uncoupled problems. The only thing that matters is a good definition of the association between the coupled problems and the proper order for solving the equations. To calculate temperature, a transient simulation must be implemented [57].

Many schemes with various levels of complexity and stability can be used to solve this coupled problem. Some of the most famous are the Crank–Nicholson, Implicit Euler, and Explicit Euler methods. Crank–Nicholson and Explicit Euler are predefined in GetDP. One of the major differences between these schemes is the method used. Crank–Nicolson and Explicit Euler used an explicit resulting method. They typically use various predictor-corrector formulations, where the value of a function in the future time step $f(t_{n+1})$ is predicted and then corrected by solving the system of non-linear equations. This is a costly and slow process, particularly with higher-order schemes. The advantage of these schemes is the solution stability, which does not depend on the size of the time step.

The Explicit Euler method is a simple and fast explicit scheme. For each time step, we solve the equations and use the solution in the next time step. The electric field must

be solved for each time step because the material parameters are temperature dependent, as shown in Equations (16) and (17). The time derivative at a particular time step can be determined using the first-order approximation of the first partial derivative as follows:

$$\frac{df}{dt}(t_n) \approx \frac{f(t_n) - f(t_{n-1})}{\Delta t},$$

(20)

where $f(t_n)$ represents a function that contains the value of interest, the temperature in this case, which is calculated at this time step, and $f(t_{n-1})$ is already known from the previous time step. The Explicit Euler scheme uses known and calculated values. The problem with the Explicit Euler equation is the accuracy of the approximation in (20), which is directly correlated with the size of the time step. Smaller time steps yield smaller errors, but they increase the number of time steps and, consequently, the duration of the simulation. In GetDP, predefined variables such as \$Time, \$DTime, and \$TimeStep, which define the current time, current time increment, and current time step, respectively, are necessary for the construction, control, and modification of the transient schemes. The time step value that ensures numerical stability can be determined by calculating the largest eigenvalue of the global thermal stiffness over the global thermal mass values [58,59]. This process is computationally expensive for large thermal matrices [58].

The optimal solution is to have a reasonable starting value for the time step as a fraction of the total observed time, and then use the test function to check the change in the observed value in comparison with the previous time step and adapt the time step size. If the change is greater than the specified value, we can repeat the time loop with a smaller time step and use this simple iterative procedure until the condition is satisfied.

In this study, we defined four points inside the heat domain (liver and tumor) in which we observed the calculated temperature (see Figure 3a). Points A, B, C, and D are in the plane with maximum transverse and longitudinal dimensions [10,13]. The initial temperature of the heat domain was set at 37 °C. If the absolute temperature difference between successive time steps is larger than one, the loop repeats with a halved time step. Tests will occur at the defined time values. The starting time step was 10 s, and the value of 2.5 s in the current models satisfied the defined conditions.

After obtaining the temperature, we were particularly interested in calculating the tissue damage estimated using Equation (19). The standard approach is to define a third system of coupled equations to calculate the time integration of Equation (18). This is not necessary, and powerful post-processing functionality and post-operation objects can be used [45]. Any calculated unknown can be used to define expressions, such as the integration of the calculated unknown through the surface or volume. In post-processing, the result of the expression can be written as an internal variable and used in the next time step. We can use a simple scalar value (for the temperature at a specific point in the domain) or a matrix calculated across the entire domain (for the definition of the temperature values in the heat domain).

$$C_i = Ae^{\left(-\frac{\Delta E}{RT_i}\right)},$$

(21)

$$\Omega = \int_0^T C\,dt = \int_0^{\Delta T} C_1\,dt + \int_{\Delta T}^{2\Delta T} C_2\,dt + \cdots + \int_{(N-1)\Delta T}^{N\Delta T} C_N\,dt = C_1\Delta T + C_2\Delta T + \cdots + C_N\Delta T.$$

(22)

For tissue damage, the equation is very simple, and all values inside the integral are known and constant C_i in Equation (21). In the observed time steps $(C_1, C_2, \ldots, C_N)$, we can simply add a call inside the time loop for post-processing, which stores the calculated $C_1\Delta T$. In the next time step, we add the calculated $C_2\Delta T$, and so on, until the final step is completed, as in Equation (22). At each time step, we used a current value of Ω in θ_d to obtain the fraction of necrotic tissue. One particular aspect that needs to be addressed is that, while values are known, there are multiple exponents in the expressions that can produce extremely large values. Calculations using coupled equations are particularly sensitive

and can easily break the entire numerical approximation. The maximum exponent value that can be used in the double-precision floating-point format is 2^{1023}, and the minimum exponent value is 2^{-1022}. In θ_d, this can be exceeded, which would cause errors; therefore, we can limit the maximal value of Ω which can be used for θ_d, as a simple expression, such as if $\Omega > 10$, we use $\Omega = 10$. Factor e^{-10} has a very small value, and in this case, there is not much difference if an even smaller value is used since, here, $\theta_d \approx 1$, which indicates total tissue necrosis.

The simulation was performed using a SuperMicro workstation with a Threadripper 3975WX processor. A comparison of the simulation parameters for the two meshing types is presented in Table 5. The degree of freedom (DOF) in the FEM represents the number of unknowns. This depends on the type of elements used (number of nodes) and the number of dependent variables.

Table 5. Comparison of the DOFs for the electric field (E) and temperature (T), elements, and time per iteration, for model with unstructured and mixed meshing.

	DOF T	DOF E	Hexahedron	Tetrahedron	Pyramids	Time
Unstructured	68,449	697,730	0	639,658	0	170 s
Mixed	67,573	274,352	49,552	99,063	2709	47 s

It should be noted that the volume of the geometry with mixed meshing is 27% larger than the volume of the geometry with unstructured meshing, but again, we can see that the number of DOFs for the temperature calculation is smaller for 876 and 2.54 times smaller for the electric field calculation. Thus, the simulation time is 3.62 times faster for mixed meshing.

The SAR simulation is shown in Figure 10. In both models, the results were identical. The SAR results essentially represent the MWA propagation and shape. The SAR shape was symmetrical and spherical in all planes, and the strongest intensity was in the proximity of the antenna slots.

In Figure 11, we can see a fast growth of the ablation area until 360 s, after which the growth is much subtler. The tumor area and temperature isocontours correspond to areas at approximately 50 °C and 60 °C, respectively. Above 60 °C, rapid cell death would happen [10]. Temperatures above 42 °C for moderate periods cause damage to cellular functions [14]. The level of damage depends on temperature and duration of exposure. At 600 s, the entire tumor was at 50 °C, which was sufficient for its destruction.

Figure 12 shows the actual ablation shape calculated using Equation (22). This follows the rise in temperature and saturation patterns. At 600 s, the entire tumor was in the ablation area with a fraction of tissue damage close to 1, which accounts for total necrosis.

The fraction of necrotic tissue damage at 600 s for multiple planes and for both meshing models is shown in Figure 13. The shape of the MWA follows the same pattern as that of the SAR, and they are visually identical. The tumor was completely located in an area of total necrosis.

In Figures 14 and 15, we can see continuous estimations of the temperature, fraction of necrotic tissue, and tissue damage at four control points for mixed-meshing, since extremely small differences were observed between the two meshing models. The results were very stable, and there was no abrupt change in the values, suggesting that the time scheme used was accurate. Point D, which is near the slots, shows a very rapid rise of the temperature and achieves around 86 °C at 600 s; we can see that total necrosis happens exactly when the temperature passes 60 °C at 130 s, which is in accordance with previous reports [10]. Point B is at the edge of the tumor and has a temperature slightly below 60 °C at 600 s, while total necrosis occurs at around 350 s. Point A is near the antenna but is moved away from the slots toward the antenna port. It shows a similar temperature as point B, with a value of around 55 °C at 600 s and total necrosis at around 450 s. Point C is placed on the same axis as the antenna, but away from it and outside of the tumor, and achieves a

value of around 48 °C at 600 s. Here, the fraction of necrotic tissue damage is around 0.88 at 600 s. With additional time, total tissue damage would occur; therefore, it is essential to have an antenna that is able to cover the entire tumor in a short time frame. The MWA should originate from radiation, and extremely high temperatures around the antenna should be avoided because they can cause rapid heating of the antenna surface, causing tissue damage along the entire antenna structure.
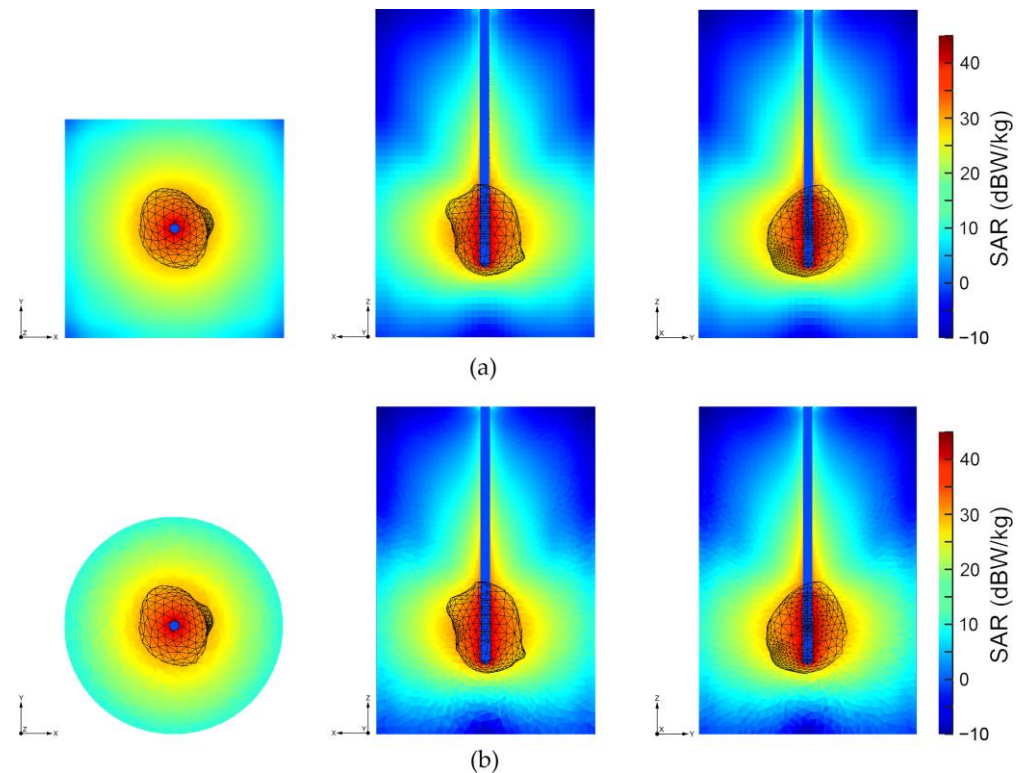

Figure 10. SAR simulation results for different cross-sections at 600 s with tumor structure designated by black color: (**a**) mixed meshing and (**b**) unstructured meshing.
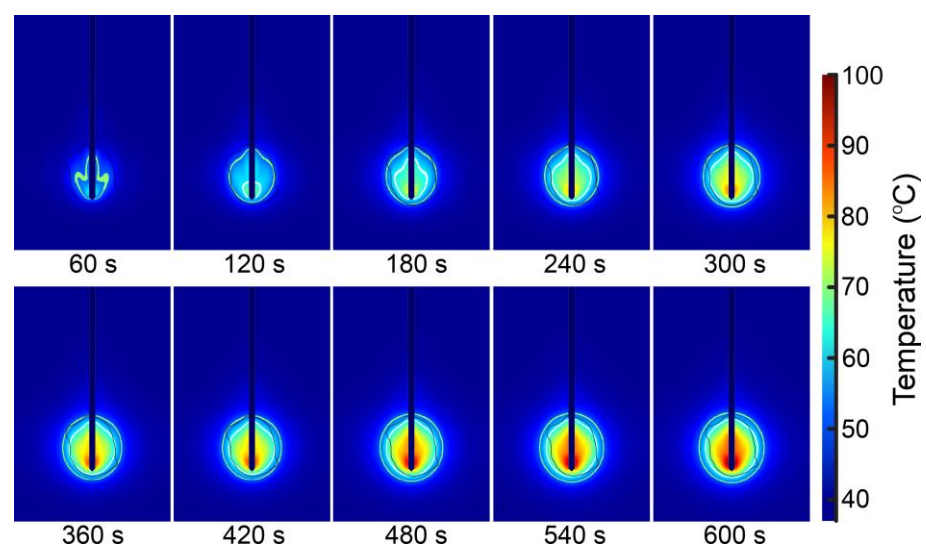

Figure 11. Temperature change with time for mixed meshing in the x-z cut plane. The tumor boundaries are marked with black lines, and the temperature isocontours corresponding to 50 °C and 60 °C are marked with light green and white, respectively.
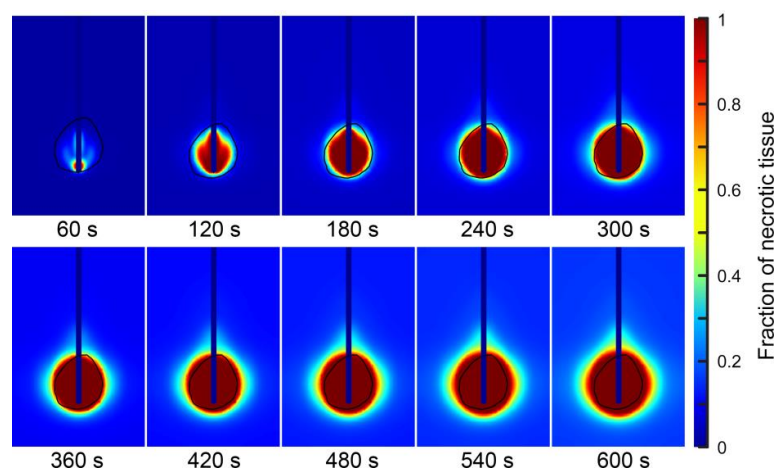
Figure 12. Fraction of the necrotic tissue change with time for mixed meshing in z-y cut plane. Tumor boundaries are marked with a black line.
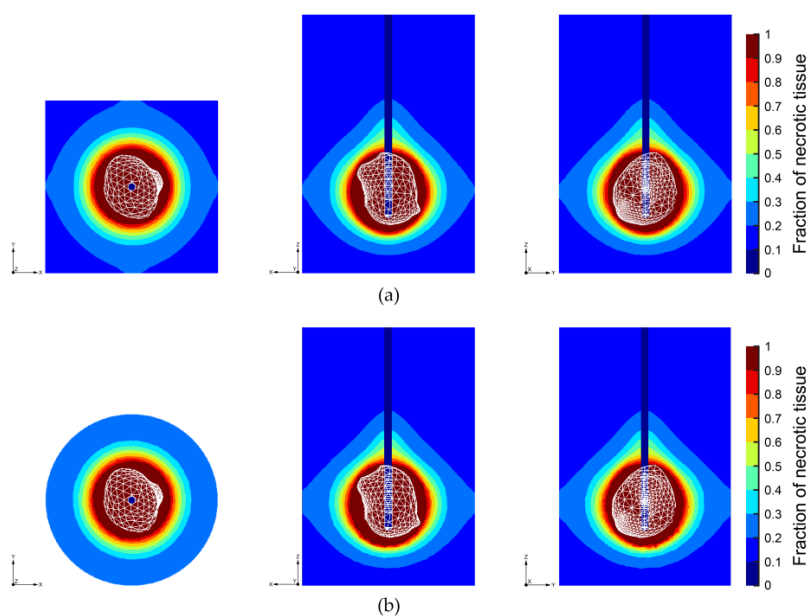

Figure 13. Fraction of necrotic tissue at different cross-sections at 600 s for (**a**) mixed meshing and (**b**) unstructured meshing. Tumor shape is designated by white color.
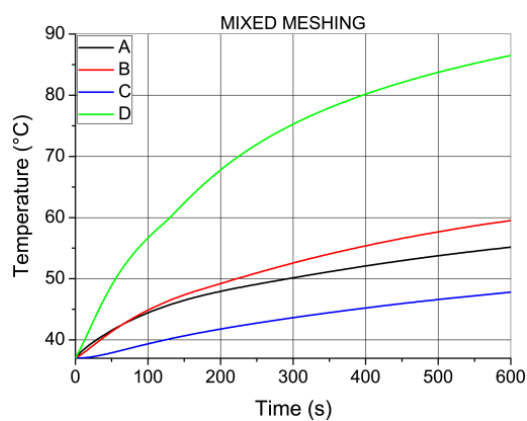

Figure 14. The dependence of temperature on time at the four points (A, B, C, and D) for mixed meshing.
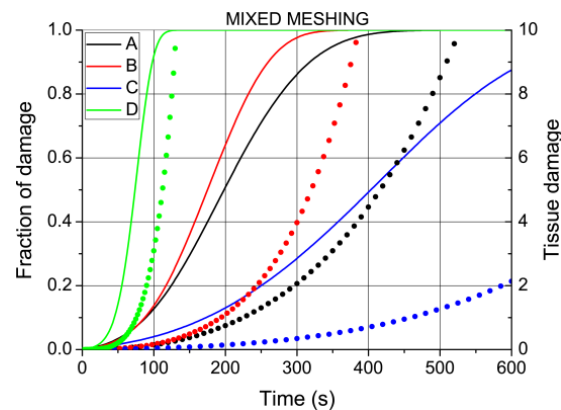
Figure 15. The fraction of necrotic tissue changes with time at the four points (A, B, C, and D) for mixed meshing (full lines) and tissue damage (dots of the same color).

4. Discussion

The tissue damage parameter is sometimes used for the estimation of damage during MWA [60,61]. The value of $\Omega = 10$ is equivalent to the value of 0.99995 for the fraction of necrotic damage, which in practice can be considered as 1 or 100% cell damage; hence, values of Ω above 10 do not add a significant change in the fraction of necrotic damage [60,62]. In MWA, there are two general objectives: irreversible damage to tumor cells and minimal damage to the surrounding healthy tissue. Two expressions were used to estimate the damage to healthy tissue. The volumetric damage (VD) is calculated as the ratio of the volume of the damaged healthy tissue ($V_{DAMAGED}$) and tumor tissue (V_{TUMOR}) [60,63]:

$$VD = \frac{V_{DAMAGED}}{V_{TUMOR}} \cdot 100\%. \tag{23}$$

The amount of damaged healthy tissue (DT) was calculated as the ratio between the volume of the damaged healthy tissue and the total volume of the liver (V_{LIVER}) without tumor tissue (V_{TUMOR}) [64,65]:

$$DT = \frac{V_{DAMAGED}}{V_{LIVER} - V_{TUMOR}} \cdot 100\%. \tag{24}$$

The boundary of damaged healthy tissue was estimated by using different parameters. The most common is the volume of the tissue inside certain limits of tissue damage, such as $\Omega \geq 4$ or $\Omega \geq 4.6$, which corresponds to 98.17% and 98.99% of the cell damage, respectively [60–65]. In this study, the volume of the tumor was 5.38 cm^3, and the volume of the tissue inside the $\Omega \geq 4.6$ was 7.13 cm^3. Thus, the volumetric damage was $(7.13 - 5.38)/5.38 = 32.53\%$. The mean volume of the human liver is around 1750 cm^3 [66]; hence, the amount of damaged healthy tissue, in this case, was $0.175/1750 = 0.1\%$, which is negligible.

In the MWA simulation, there would generally be two convergence operations. One relates to whether mesh refinement yield changes in the observed quantity below certain limits, and the second one relates to the stability of the time loop, which is related to the size of the used time step. The convergence criterion for the time loop is that the absolute value of the temperature change, calculated in control points between successive time steps, is below 1. This is implemented directly in the Explicit Euler scheme; resulting curves are stable, there is no abrupt change, and curves have a similar shape as the one in the related literature obtained with commercial software.

Mesh convergence represents a standard topic in the FEM simulation. This was related to the effect of the smaller size of the finite elements used in the solution. The convergence criterion corresponds to the maximum variation in the observed solution between simulations involving smaller finite elements. It is typically set as the relative

change (e.g., 1%). Thus, the estimation of convergence involves multiple full simulations with successive mesh refinement steps. Mesh refinement is typically performed in an adaptive manner, where parts of the volume with a higher variation of the observed quantity, between successive refinement steps, are meshed with more elements in the next step [25]. Increasing the number of elements will have a significant effect on the simulation time, and with sufficient refinement steps, it will eventually reach the limit of the available computation resources, so the number of iterations is typically limited. In the current model, we did not use mesh refinement after the FEM calculation began. In order to estimate how our mesh settings were based on limiting the maximal element size to 2 mm, compared to the mesh model generated with smaller finite elements, we repeated the simulation of the model with mixed meshing with a maximal element size of 1 mm, as shown in Figure 16. This resulted in a massive increase in the number of elements and the simulation time, as listed in Table 6.
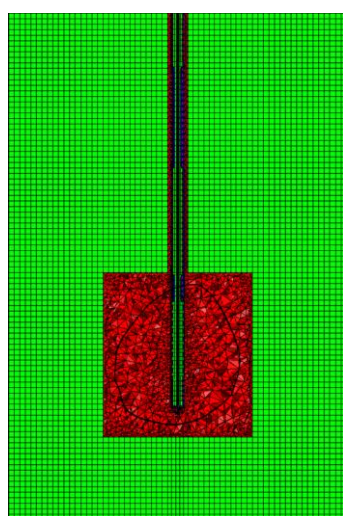

Figure 16. Meshing of the model with mixed meshing for a maximal element size of 1 mm and the same projection of the same model for a maximum element size of 2 mm are shown in Figure 8a.

Table 6. Comparison of the DOFs for the electric field (E) and temperature (T), elements, and time per iteration for models with mixed meshing and maximal mesh element sizes of 1 mm and 2 mm, respectively.

	DOF T	DOF E	Hexahedron	Tetrahedron	Pyramids	Time
1 mm	399,449	1,328,615	352,623	196,577	7389	393 s
2 mm	67,573	274,352	49,552	99,063	2709	47 s

The total number of DOFs is 1,728,064 in this case, which is more than five times as many compared to the previous case, and the total number of elements is 3.68 times higher. The simulation time is 8.36 times longer. The temperature obtained at the control points from this simulation was compared with the previous one, as can be seen in Figure 17. The relative absolute temperature difference (*Ratd*) was calculated as

$$Ratd = \frac{|T_{2mm} - T_{1mm}|}{T_{2mm}} \cdot 100\%, \tag{25}$$

where T_{2mm} and T_{1mm} are the temperature values at the control point for the models with maximal mesh sizes of 2 mm and 1 mm, respectively. As shown in Figure 17, the maximal absolute relative temperature difference is around 0.2% which is acceptable in this and most other models, and is below the typically desired value of 1% [60,67]. Hence, the new

mesh model does not give any significant difference compared to the initial one, at the cost of much more DOFs and simulation time.
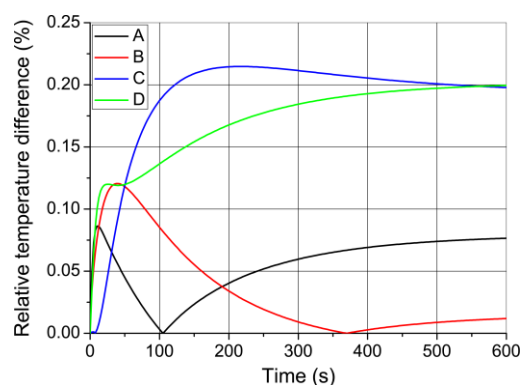

Figure 17. Relative absolute temperature difference in control points during MWA simulation for model with mixed meshing when the maximal size of finite elements is 1 mm and 2 mm.

5. Conclusions

In this study, we demonstrated that all steps in the modeling and simulation of MWA can be replaced with open-source solutions [33–47]. The geometry of a multi-slot coaxial antenna [10,13] is created using the open-source solution Gmsh [33], and the geometry of the real tumor is constructed in Gmsh from a CT scan of a patient [26]. We presented a detailed meshing procedure for both mixed and unstructured meshing [32] using Gmsh, and a significant advantage of mixed meshing is displayed. Simulation of MWA requires the calculation of the electromagnetic field and tissue heating as a coupled problem. Tissue heating is an extremely slow process in comparison with electric field propagation; therefore, we calculated the electric field in the frequency domain, and we used these results to calculate the temperature distribution in the time domain. To solve equations describing the physics of MWA, we used the FEM method implemented in the open-source solution GetDP [45,46]. Solving the coupled equations for the electric field and bio-heat is difficult, and the best approach is to solve the equations for the electric field and then use the solution in the bio-heat equation as an external heat source. In this manner, there is no difference in solving coupled problems compared to uncoupled problems. To calculate the temperature, a transient simulation was required [57]. There are many schemes with various levels of complexity and stability to solve this coupled problem, such as the Crank–Nicholson, implicit Euler, and explicit Euler schemes. One of the major differences between these schemes is the time-stepping method used. The explicit Euler method is a simple and fast explicit scheme based on using known values from the current and previous time steps, but the problem can be the accuracy of the approximation, which is directly correlated with the size of the time step. The time-step value that ensures numerical stability can be determined by calculating the largest eigenvalue of the global thermal stiffness over the global thermal mass values [58,59]. This process is computationally expensive for large thermal matrices [58]. We derived a custom, fully explicit, accurate, and stable time scheme based on an Explicit Euler, which is much faster than implicit schemes and has a considerably lower usage of computational resources.

The results presented in this paper agree well with our previously published results (temperature, microwave powers, and time of exposure) obtained using the COMSOL Multiphysics software package [25]. One of the main goals of this paper is to demonstrate that this type of simulation can be performed successfully using open-source software. The novelty of this study is the accurate modeling of the full MWA process, which is on par with commercial software such as COMSOL Multiphysics [25]. Our approach includes a superior meshing procedure designed to significantly reduce computational time and memory requirements, and a fully explicit stable Euler scheme for temperature time marching based on carefully chosen control points. The limitation of the presented

algorithm is the fact that we used the simplest tissue model. In future work, the complete model of MWA with multiple antennas and domain decomposition algorithm to achieve a significant reduction in the simulation time through parallelization will be implemented. More complex effects, such as a change in the interstitial space (porosity) of tissue during MWA, will be studied.

Author Contributions: Conceptualization, N.B., B.R. and M.R.-R.; methodology, N.B. and B.R.; software, N.B. and B.R.; investigation and data interpretation, N.B. and B.R.; original draft preparation, N.B., B.R. and M.R.-R.; writing—review, and editing, all of the authors; supervision, B.R. and M.R.-R. All authors have read and agreed to the published version of the manuscript.

Data Availability Statement: The data are available from the corresponding authors upon reasonable request.

Conflicts of Interest: The authors declare no conflict of interest.

References

1. Villanueva, A. Hepatocellular Carcinoma. *N. Engl. J. Med.* **2019**, *380*, 1450–1462. [CrossRef]
2. Arnold, M.; Abnet, C.C.; Neale, R.E.; Vignat, J.; Giovannucci, E.L.; McGlynn, K.A.; Bray, F. Global Burden of 5 Major Types of Gastrointestinal Cancer. *Gastroenterology* **2020**, *159*, 335–349. [CrossRef]
3. Llovet, J.M.; Kelley, R.K.; Villanueva, A.; Singal, A.G.; Pikarsky, E.; Roayaie, S.; Lencioni, R.; Koike, K.; Zucman-Rossi, J.; Finn, R.S. Hepatocellular carcinoma. *Nat. Rev. Dis. Prim.* **2021**, *7*, 6. [CrossRef]
4. Radmilović-Radjenović, M.; Radjenović, D.; Radjenović, B. Finite element analysis of the effect of microwave ablation on the liver, lung, kidney, and bone malignant tissues. *Europhys. Lett.* **2021**, *135*, 3500. [CrossRef]
5. Izzo, F.; Granata, V.; Grassi, R.; Fusco, R.; Palaia, R.; Delrio, P.; Carrafiello, G.; Azoulay, D.; Petrillo, A.; Curley, S.A. Radiofrequency Ablation and Microwave Ablation in Liver Tumors: An Update. *Oncologist* **2019**, *24*, e990–e1005. [CrossRef] [PubMed]
6. Tan, W.; Deng, Q.; Lin, S.; Wang, Y.; Xu, G. Comparison of microwave ablation and radiofrequency ablation for hepatocellular carcinoma: A systematic review and meta-analysis. *Int. J. Hyperth.* **2019**, *36*, 264–272. [CrossRef] [PubMed]
7. Li, W.; Ni, C.F. Current status of the combination therapy of transarterial chemoembolization and local ablation for hepatocellular carcinoma. *Abdom. Radiol.* **2019**, *44*, 2268–2275. [CrossRef] [PubMed]
8. Hojjatollah, F.; Punit, P. Antenna Designs for Microwave Tissue Ablation. *Crit. Rev. Biomed. Eng.* **2018**, *46*, 495–521. [CrossRef]
9. Huang, H.; Zhang, L.; Moser, M.A.J.; Zhang, W.; Zhang, B. A review of antenna designs for percutaneous microwave ablation. *Phys. Med.* **2021**, *84*, 254–264. [CrossRef]
10. Ge, M.; Jiang, H.; Huang, X.; Zhou, Y.; Zhi, D.; Zhao, G.; Chen, Y.; Wang, L.; Qiu, B. A multi-slot coaxial microwave antenna for liver tumor ablation. *Phys. Med. Biol.* **2018**, *63*, 175011. [CrossRef]
11. Wang, T.; Zhao, G.; Qiu, B. Theoretical evaluation of the treatment effectiveness of a novel coaxial multi-slot antenna for conformal microwave ablation of tumors. *Int. J. Heat Mass Transf.* **2015**, *90*, 81–91. [CrossRef]
12. Vogl, T.J.; Basten, L.M.; Nour-Eldin, N.-E.A.; Kaltenbach, B.; Bodelle, B.; Wichmann, J.L.; Ackermann, H.; Naguib, N.N.N. Evaluation of microwave ablation of liver malignancy with enabled constant spatial energy control to achieve a predictable spherical ablation zone. *Int. J. Hyperth.* **2018**, *34*, 492–500. [CrossRef]
13. Radjenović, B.; Sabo, M.; Šoltes, L.; Prnova, M.; Čičak, P.; Radmilović-Radjenović, M. On Efficacy of Microwave Ablation in the Thermal Treatment of an Early-Stage Hepatocellular Carcinoma. *Cancers* **2021**, *13*, 5784. [CrossRef]
14. Tehrani, M.H.H.; Soltani, M.; Kashkooli, F.M.; Raahemifar, K. Use of microwave ablation for thermal treatment of solid tumors with different shapes and sizes—A computational approach. *PLoS ONE* **2020**, *15*, e0233219. [CrossRef]
15. Radmilović-Radjenović, M.; Bošković, N.; Radjenović, B. Computational Modeling of Microwave Tumor Ablation. *Bioengineering* **2022**, *9*, 656. [CrossRef] [PubMed]
16. Radmilović-Radjenović, M.; Sabo, M.; Prnova, M.; Šoltes, L.; Radjenović, B. Finite Element Analysis of the Microwave Ablation Method for Enhanced Lung Cancer Treatment. *Cancers* **2021**, *13*, 3500. [CrossRef]
17. Radmilović-Radjenović, M.; Bošković, N.; Sabo, M.; Radjenović, B. An Analysis of Microwave Ablation Parameters for Treatment of Liver Tumors from the 3D-IRCADb-01 Database. *Biomedicines* **2022**, *10*, 1569. [CrossRef]
18. Ji, Z.; Brace, C.L. Expanded modeling of temperature-dependent dielectric properties for microwave thermal ablation. *Phys. Med. Biol.* **2011**, *56*, 5249. [CrossRef] [PubMed]
19. Rossmann, C.; Haemmerich, D. Review of temperature dependence of thermal properties, dielectric properties, and perfusion of biological tissues at hyperthermic and ablation temperatures. *Crit. Rev. Biomed. Eng.* **2014**, *42*, 467–492. [CrossRef] [PubMed]
20. Taeprasartsit, P.; Pathompatai, C.; Jusomjai, K.; Wibowo, H.; Sebek, J.; Prakash, P. A personalized approach for microwave ablation treatment planning fusing radiomics and bioheat transfer modeling. *Proc. SPIE* **2020**, *11315*, 780–795. [CrossRef]

21. Hossan, M.R.; Dutta, P. Effects of temperature dependent properties in electromagnetic heating. *Int. J. Heat. Mass. Transf.* **2012**, *55*, 3412–3422. [CrossRef]

22. O'Rourke, A.P.; Lazebnik, M.; Bertram, J.M.; Converse, M.C.; Hagness, S.C.; Webster, J.G.; Mahvi, D.M. Dielectric properties of human normal, malignant and cirrhotic liver tissue: In vivo and ex vivo measurements from 0.5 to 20 GHz using a precision open-ended coaxial probe. *Phys. Med. Biol.* **2007**, *52*, 4707–4719. [CrossRef]

23. Andreozzi, A.; Iasiello, M.; Tucci, C. An overview of mathematical models and modulated-heating protocols for thermal ablation. *Adv. Heat Transf.* **2020**, *52*, 489–541. [CrossRef]

24. Heat Transfer Modeling Software for Analyzing Thermal Effects. Available online: https://www.comsol.com/heat-transfer-module/ (accessed on 6 February 2023).

25. COMSOL—Software for Multiphysics Simulation. Available online: https://www.comsol.com/ (accessed on 6 February 2023).

26. 3D-IRCADb. Available online: https://www.ircad.fr/research/3dircadb/ (accessed on 6 February 2023).

27. Kiah, M.L.M.; Haiqi, A.; Zaidan, B.B.; Zaidan, A.A. Open source EMR software: Profiling, insights and hands-on analysis. *Comput. Methods Programs Biomed.* **2014**, *117*, 360–382. [CrossRef]

28. Delp, S.L.; Anderson, F.C.; Arnold, A.S.; Loan, P.; Habib, A.; John, C.T.; Guendelman, E.; Thelen, D.G. OpenSim: Open-source software to create and analyze dynamic simulations of movement. *IEEE Trans. Biomed. Eng.* **2007**, *54*, 1940–1950. [CrossRef]

29. Cross, D.E.; Bauer, T.M.; Tchantchaleishvili, V. 3D organ modeling with open-source software. *Artif. Organs* **2019**, *43*, 596–598. [CrossRef] [PubMed]

30. Schmitz, A.; Piovesan, D. Development of an Open-Source, Discrete Element Knee Model. *IEEE Trans. Biomed. Eng.* **2016**, *63*, 2056–2067. [CrossRef] [PubMed]

31. Jian-Ming, J. *Theory and Computation of Electromagnetic Fields*, 2nd ed.; John Wiley & Sons, Inc.: Hoboken, NJ, USA, 2015.

32. Frey, P.J.; George, P.-L. *Mesh Generation: Application to Finite Elements*, 2nd ed.; John Wiley & Sons, Inc.: Hoboken, NJ, USA, 2008.

33. Geuzaine, C.; Remacle, J.-F. Gmsh: A three-dimensional finite element mesh generator with built-in pre- and post-processing facilities. *Int. J. Numer. Meth. Eng.* **2009**, *79*, 1309–1331. [CrossRef]

34. Remacle, J.-F.; Geuzaine, C.; Compère, G.; Marchandise, E. High-quality surface remeshing using harmonic maps. *Int. J. Numer. Meth. Eng.* **2010**, *83*, 403–425. [CrossRef]

35. Marchandise, E.; de Wiart, C.C.; Vos, W.G.; Geuzaine, C.; Remacle, J.-F. High-quality surface remeshing using harmonic maps—Part II: Surfaces with high genus and of large aspect ratio. *Int. J. Numer. Meth. Eng.* **2011**, *86*, 1303–1321. [CrossRef]

36. Marchandise, E.; Remacle, J.-F.; Geuzaine, C. Optimal parametrizations for surface remeshing. *Eng. Comput.* **2014**, *30*, 383–402. [CrossRef]

37. Remacle, J.-F.; Lambrechts, J.; Seny, B.; Marchandise, E.; Johnen, A.; Geuzainet, C. Blossom-Quad: A non-uniform quadrilateral mesh generator using a minimum-cost perfect-matching algorithm. *Int. J. Numer. Meth. Eng.* **2012**, *89*, 1102–1119. [CrossRef]

38. Remacle, J.-F.; Henrotte, F.; Carrier-Baudouin, T.; Béchet, E.; Marchandise, E.; Geuzaine, C.; Mouton, T. A frontal Delaunay quad mesh generator using the $L\infty$ norm. *Int. J. Numer. Meth. Eng.* **2013**, *94*, 494–512. [CrossRef]

39. Johnen, A.; Remacle, J.-F.; Geuzaine, C. Geometric validity of curvilinear finite elements. *J. Comput. Phys.* **2013**, *233*, 359–372. [CrossRef]

40. Johnen, A.; Remacle, J.-F.; Geuzaine, C. Geometric validity of high-Order triangular finite elements. *Eng. Comput.* **2014**, *30*, 375–382. [CrossRef]

41. Toulorge, T.; Geuzaine, C.; Remacle, J.-F.; Lambrechts, J. Robust untangling of curvilinear meshes. *J. Comput. Phys.* **2013**, *254*, 8–26. [CrossRef]

42. Remacle, J.-F.; Chevaugeon, N.; Marchandise, E.; Geuzaine, C. Efficient visualization of high-order finite elements. *Int. J. Numer. Meth. Eng.* **2006**, *69*, 750–771. [CrossRef]

43. Geuzaine, C.; Remacle, J.-F. Gmsh Reference Manual, A Three-Dimensional Finite Element Mesh Generator with Built-in Pre- and Post-Processing Facilities. Available online: https://gmsh.info/ (accessed on 6 February 2023).

44. Open CASCADE Technology. Available online: https://dev.opencascade.org/ (accessed on 6 February 2023).

45. Dular, P.; Geuzaine, C. GetDP Reference Manual: The Documentation for GetDP, A General Environment for the Treatment of Discrete Problems. Available online: https://getdp.info/ (accessed on 6 February 2023).

46. Dular, P.; Geuzaine, C.; Henrotte, F.; Legros, W. A general environment for the treatment of discrete problems and its application to the finite element method. *IEEE Trans. Magn.* **1998**, *34*, 3395–3398. [CrossRef]

47. ONELAB: Open Numerical Engineering Laboratory. Available online: https://onelab.info/ (accessed on 6 February 2023).

48. Pennes, H.H. Analysis of tissue and arterial blood temperatures in the resting human forearm. *J. Appl. Physiol.* **1948**, *1*, 93–122. [CrossRef]

49. Gillies, R.J.; Schornack, P.A.; Secomb, T.W.; Raghunand, N. Causes and effects of heterogeneous perfusion in tumors. *Neoplasia* **1999**, *1*, 197–207. [CrossRef]

50. Sweeney, P.W.; d'Esposito, A.; Walker-Samuel, S.; Shipley, R.J. Modelling the transport of fluid through heterogeneous, whole tumours in silico. *PLoS Comput. Biol.* **2019**, *15*, e1006751. [CrossRef] [PubMed]

51. Chartampilas, E.; Rafailidis, V.; Georgopoulou, V.; Kalarakis, G.; Hatzidakis, A.; Prassopoulos, P. Current Imaging Diagnosis of Hepatocellular Carcinoma. *Cancers* **2022**, *14*, 3997. [CrossRef]

52. Kim, S.H.; Kamaya, A.; Willmann, J.K. CT Perfusion of the Liver: Principles and Applications in Oncology. *Radiology* **2014**, *272*, 322–344. [CrossRef] [PubMed]

53. Cavagnaro, M.; Pinto, R.; Lopresto, V. Numerical models to evaluate the temperature increase induced by ex vivo microwave thermal ablation. *Phys. Med. Biol.* **2015**, *60*, 3287–3311. [CrossRef] [PubMed]

54. Yang, D.; Converse, M.C.; Mahvi, D.M.; Webster, J.G. Expanding the Bioheat Equation to Include Tissue Internal Water Evaporation during Heating. *IEEE Trans. Biomed. Eng.* **2007**, *54*, 1382–1388. [CrossRef]

55. Berjano, E.J. Theoretical modeling for radiofrequency ablation: State-of-the-art and challenges for the future. *BioMed Eng. Online* **2006**, *5*, 24. [CrossRef]

56. Selmi, M.; Bin Dukhyil, A.A.; Belmabrouk, H. Numerical Analysis of Human Cancer Therapy Using Microwave Ablation. *Appl. Sci.* **2020**, *10*, 211. [CrossRef]

57. Gartling, D.K.; Reddy, J.N. *The Finite Element Method in Heat Transfer and Fluid Dynamics*, 3rd ed.; CRC Press: Boca Raton, FL, USA; Taylor & Francis Group: Abingdon, UK, 2010.

58. Zhang, J.; Chauhan, S. Real-time computation of bio-heat transfer in the fast explicit dynamics finite element algorithm (FED-FEM) framework. *Numer. Heat Transf. Part B Fundam.* **2019**, *75*, 217–238. [CrossRef]

59. Rong, X.; Niu, R.; Liu, J. Stability analysis of smoothed finite element methods with explicit method for transient heat transfer problems. *Int. J. Comput. Methods* **2018**, *17*, 1845005. [CrossRef]

60. Singh, M.; Singh, T.; Soni, S. Pre-operative Assessment of Ablation Margins for Variable Blood Perfusion Metrics in a Magnetic Resonance Imaging Based Complex Breast Tumour Anatomy: Simulation Paradigms in Thermal Therapies. *Comput. Methods Programs Biomed.* **2021**, *198*, 105781. [CrossRef]

61. Singh, M.; Gu, Q.; Ma, R.; Zhu, L. Heating Protocol Design Affected by Nanoparticle Redistribution and Thermal Damage Model in Magnetic Nanoparticle Hyperthermia for Cancer Treatment. *ASME J. Heat Transfer.* **2020**, *142*, 072501. [CrossRef]

62. Pearce, J.A. Comparative analysis of mathematical models of cell death and thermal damage processes. *Int. J. Hyperth.* **2013**, *29*, 262–280. [CrossRef] [PubMed]

63. LeBrun, A.; Ma, R.; Zhu, L. MicroCT image based simulation to design heating protocols in magnetic nanoparticle hyperthermia for cancer treatment. *J. Therm. Biol.* **2016**, *62*, 129–137. [CrossRef]

64. Zhang, B.; Moser, M.A.J.; Zhang, E.M.; Luo, Y.; Zhang, H.; Zhang, W. Study of the relationship between the target tissue necrosis volume and the target tissue size in liver tumours using two-compartment finite element RFA modelling. *Int. J. Hyperth.* **2014**, *30*, 593–602. [CrossRef] [PubMed]

65. Manuchehrabadi, N.; Zhu, L. Development of a computational simulation tool to design a protocol for treating prostate tumours using transurethral laser photothermal therapy. *Int. J. Hyperth.* **2014**, *30*, 349–361. [CrossRef] [PubMed]

66. Lodewick, T.M.; Arnoldussen, C.W.; Lahaye, M.J.; van Mierlo, K.M.; Neumann, U.P.; Beets-Tan, R.G.; Dejong, C.H.; van Dam, R.M. Fast and accurate liver volumetry prior to hepatectomy. *HPB (Oxford)* **2016**, *18*, 764–772. [CrossRef]

67. Singh, M.; Ma, R.; Zhu, L. Quantitative evaluation of effects of coupled temperature elevation, thermal damage, and enlarged porosity on nanoparticle migration in tumors during magnetic nanoparticle hyperthermia. *Int. Commun. Heat Mass Transf.* **2021**, *126*, 105393. [CrossRef]